

Electric field control of anomalous Hall effect in $\text{CaIrO}_3/\text{CaMnO}_3$ heterostructureR. Nishino,¹ T. C. Fujita,^{1, a)} and M. Kawasaki^{1, 2}¹⁾*Department of Applied Physics and Quantum Phase Electronics Center, University of Tokyo, Tokyo 113-8656, Japan*²⁾*RIKEN Center for Emergent Matter Science (CEMS), Wako 351-0198, Japan*

(Dated: 5 August 2022)

We demonstrate an electric field control of anomalous Hall effect emerging in $\text{CaIrO}_3/\text{CaMnO}_3$ heterostructures. We fabricate both electron-type and hole-type carrier samples by tuning epitaxial strain and then control the carrier density in CaIrO_3 layer via electric double layer gating technique. As the Fermi energy of CaIrO_3 is tuned close to the Dirac line node, anomalous Hall conductivity is enlarged in both carrier-type samples. This result reveals that the anomalous Hall effect comes from the intrinsic origin reflecting the Dirac like dispersion in CaIrO_3 . We propose that band splitting induced by the interface ferromagnetism yields several band crossing points near the Dirac line node. These points play as a source of the Berry curvature and contribute to the anomalous Hall effect.

PACS numbers: 72.15.Gd, 73.50.-h, 75.47.-m, 75.47.Lx, 81.15.-z

arXiv:2208.02479v1 [cond-mat.str-el] 4 Aug 2022

^{a)}Electronic mail: fujita@ap.t.u-tokyo.ac.jp

Oxide heterointerfaces exhibit a variety of exotic physical properties due to complex interplay between charge, spin and orbital degrees of freedom across the interface [1–3]. In particular, interface ferromagnetism driven by charge transfer is one of the well-known examples. Ferromagnetism emerges at various interfaces between two non-ferromagnetic compounds; for example, manganites with an antiferromagnetic insulator ground state (CaMnO_3 , SrMnO_3) and paramagnetic conductors (CaRuO_3 , SrIrO_3 , etc.) [4–7]. When these materials with different chemical potentials are adjacent to each other, electrons are injected into originally empty e_g orbitals of Mn^{4+} to adjust both chemical potentials [8]. This leads to an intrinsic doping of electrons to manganites and assists double exchange interaction. As a result of competition between the double-exchange interaction near the interface and superexchange interaction in the bulk region, the system takes a canted anti-ferromagnetic state and exhibits weak ferromagnetism.

This interface ferromagnetism in turn gives rise to anomalous Hall effect (AHE), which is experimentally verified in $\text{SrIrO}_3/\text{SrMnO}_3$ superlattices with short period [5]. Theoretical calculation predicts that the AHE is intrinsic effect where electrons acquire anomalous Hall velocity induced by the Berry curvature [9]. In this context, it is interesting to modulate the strength of spin-orbit interaction or carrier density (i.e., the position of the Fermi energy) by an external electric field, since the magnitude of the anomalous Hall conductivity (AHC) is linked to these parameters [10]. However, an electric field modulation is difficult for $\text{SrIrO}_3/\text{SrMnO}_3$ superlattices because the electric field cannot uniformly modulate every interfaces due to the screening effect, which prohibits us from studying the electric field effect on the AHE emerged at the interface.

In this study, we investigate an electric field effect on AHE in $\text{CaIrO}_3/\text{CaMnO}_3$ heterostructures. For $\text{SrIrO}_3/\text{SrMnO}_3$, AHE was reported only in superlattice structure so far [5]. On the other hand, for $\text{CaIrO}_3/\text{CaMnO}_3$, emergence of AHE was reported even in bilayer structure [11]. The reported carrier density of CaIrO_3 is one or two orders of magnitude smaller than that of SrIrO_3 ; around 10^{17} cm^{-3} and 10^{19} cm^{-3} orders in bulk single crystals [12] and epitaxial thin films [13], respectively, which is more suitable for an electric field control of the Fermi energy. Furthermore, CaIrO_3 is known to be a topological semimetal, so-called nodal line semimetal, and to possess Dirac line node near the Fermi energy, wherein the conduction and valence bands cross along a closed line in momentum space. This Dirac line node imparts high-mobility carriers due to the large band dispersion

as in the case of other Dirac electron systems. Moreover, by breaking the time-reversal symmetry, degeneracy of the line node can be lifted, yielding Weyl nodes which function as sources of the Berry curvature and contribute to AHE. These features render this system an ideal platform to examine the Fermi energy dependence of AHE originating from Dirac-like band structure in oxides. We fabricate heterostructures with *n*- and *p*-type carriers by controlling epitaxial strain imposed by substrates and then modulate the carrier density in CaIrO₃ layer via electric double layer (EDL) gating method [14–17].

CaIrO₃/CaMnO₃ heterostructures were grown on (001) oriented LaAlO₃ and SrTiO₃ substrates by pulsed laser deposition. CaMnO₃ films were grown at 600 °C under 8 mTorr oxygen pressure. CaIrO₃ films were then deposited *in situ* on the CaMnO₃ at 600 °C under 40 mTorr oxygen pressure. Typical thickness of CaIrO₃ (CaMnO₃) for heterostructures is ~ 6 nm (~ 1.5 nm). Reciprocal space mappings indicate that CaIrO₃ films are fully strained to both LaAlO₃ and SrTiO₃ substrates (see Supplementary Fig. S1). For comparison of the transport properties between heterostructures and each constituent film, we also prepared 7 nm-thick CaIrO₃ and 1.5 nm-thick Ce_{0.05}Ca_{0.95}MnO₃ films on LaAlO₃ substrates. Since electrons may be injected into the CaMnO₃ in the heterostructure, we tried to mimic a similar electronic state by Ce substitution. This 5% Ce-doping corresponds to the interface charge transfer of 0.1 electron/Mn, which is comparable with those of CaRuO₃/CaMnO₃ (~ 0.08 electron/Mn) in Ref. [8] and CaIrO₃/CaMnO₃ (~ 0.11 electron/Mn) in Ref. [11]. For the Ce_{0.05}Ca_{0.95}MnO₃ film, 4 nm-thick CaTiO₃ epitaxial cap layer was deposited to avoid surface degradation. For EDL gating experiments, we employed ionic liquid (IL), N,N-diethyl-N-methyl-N-(2-methoxyethyl) N-methylammonium tetrafluoroborate (DEME-BF₄), in which a gate electrode of Pt coil was immersed. The schematic of the device structure is depicted in Fig. S2(a) of Supplementary Materials. Typical channel size for electrical transport measurements is 2×4 mm², with which the measured resistance was converted into sheet resistance (R_S). The transport properties were measured under vacuum with a back pressure of 1×10^{-5} Torr. Before the electrical measurements, the IL was stored in a vacuum hot plate at 90 °C for several hours to remove water contamination which may induce some electrochemical reactions.

We first discuss the difference of the transport properties between the heterostructure and each constituent film. There has been a report about metallic temperature dependence of resistivity and emerging AHE for compressively strained 20 nm-thick Ce_{0.05}Ca_{0.95}MnO₃ films

grown on (001) oriented YAlO_3 substrates [18]. Therefore, it is important to clarify which layer contributes to the transport phenomena in our heterostructures. Figure 1(a) shows the temperature dependence of R_S for the $\text{CaIrO}_3/\text{CaMnO}_3$ heterostructure and the CaIrO_3 film grown on LaAlO_3 substrates. The inset shows the R_S of 1.5 nm-thick $\text{Ce}_{0.05}\text{Ca}_{0.95}\text{MnO}_3$ film as a function of temperature. The behavior of R_S in the heterostructure is similar to that in the CaIrO_3 film. Both samples exhibit a semimetallic temperature dependence and the R_S moderately increases with decreasing temperature. On the other hand, the R_S of $\text{Ce}_{0.05}\text{Ca}_{0.95}\text{MnO}_3$ film is several orders of magnitude higher than that of the heterostructure and exhibits an insulating behavior as shown in Fig. 1(b), which is totally different from the $\text{Ce}_{0.05}\text{Ca}_{0.95}\text{MnO}_3$ films grown on YAlO_3 (Ref.[18]). This contrast plausibly comes from tensile strain imposed on our $\text{Ce}_{0.05}\text{Ca}_{0.95}\text{MnO}_3$ films grown on LaAlO_3 , which stabilizes an insulating ground state as reported previously [19].

In opposition to the similarity of the behavior in R_S between the heterostructure and the CaIrO_3 film, a clear difference is observed in Hall measurements. Figure 1(c) shows magnetic field (B) dependence of Hall resistance (R_{yx}) at 5 K. While the R_{yx} for the CaIrO_3 film is merely linear to B , the R_{yx} for the heterostructure exhibits a clear hysteresis, indicating the emergence of AHE due to the interface ferromagnetism. In this case, the R_{yx} can be empirically expressed by $R_{yx} = R_H B + R_{\text{AHE}}$, where the $R_H B$ (R_H : Hall coefficient) and R_{AHE} terms denote ordinary and anomalous Hall resistances, respectively. Figure 1(d) shows R_{AHE} as a function of B at various temperatures. The R_{AHE} term is extracted by subtracting the $R_H B$ from the measured R_{yx} , where the $R_H B$ term is estimated from the linear fitting in the higher magnetic field region as shown in the red broken line in Fig. 1(c). R_{AHE} emerges below ~ 60 K and exhibits an anticlockwise hysteresis at low temperature. It is worth noting that the sign of AHE is positive for the heterostructure while previously reported $\text{Ce}_{0.05}\text{Ca}_{0.95}\text{MnO}_3$ films on YAlO_3 substrates exhibits the negative sign of AHE [18].

From the comparison of the transport properties between the heterostructure and each constituent film, we have confirmed that CaIrO_3 layer is dominant in both electrical conduction and the observed AHE rather than electron doped CaMnO_3 layer in the heterostructure. Here we propose a possible mechanism of the observed AHE as follows: (i) electrons transfer from CaIrO_3 to CaMnO_3 layers and induce double-exchange interaction, resulting in a weak ferromagnetism (canted antiferromagnetism) in CaMnO_3 layer near the interface, (ii) magnetization is expected to be induced in CaIrO_3 near the interface due to magnetic proximity

effect, and (iii) CaIrO₃ layer with magnetization exhibits the AHE. In this study, it is difficult to reveal the magnetic ordering at the interface in detail only from the transport properties. However, recent experimental result and theoretical calculations for SrIrO₃/SrMnO₃ superlattice revealed that the intra-layer interaction within the SrMnO₃ and SrIrO₃ layers is ferromagnetic but the inter-layer interaction between the SrMnO₃ and SrIrO₃ layers is antiferromagnetic [5, 9, 20]. Although it is intriguing to elucidate the mechanism of the emergent ferromagnetism in CaIrO₃/CaMnO₃ heterostructures, this is beyond the scope of this report and remains as future work.

We then examine the effect of epitaxial strain on the transport properties in the heterostructures. As shown in Fig. 2(a), CaIrO₃ grown on SrTiO₃ substrates is imposed on tensile strain while that on LaAlO₃ substrates is compressively strained. Figure 2(b) shows B dependence of R_{yx} for the heterostructures grown on SrTiO₃ (blue) and LaAlO₃ (red) substrates measured at 5 K. Hall coefficient R_H exhibits opposite sign between two samples, indicating that hole (electron) type carrier is dominant for the heterostructure grown on SrTiO₃ (LaAlO₃). Previous studies report that carrier type of CaIrO₃ thin films is sensitive to epitaxial strain [13, 21]. It has been theoretically predicted that tetragonal distortion can lift the degeneracy of t_{2g} orbitals in the $J_{\text{eff}} = 1/2$ state of Ir⁴⁺ near Fermi level [22], and thus the epitaxial strain might induce this carrier type change. Yet, considering the sensitivity of the band structure of CaIrO₃ against electron correlation as well [12], further elucidation of the origin of the change in carrier type is a matter of speculation.

To obtain further insight into the origin of the observed AHE, we attempt to tune the position of the Fermi energy of CaIrO₃ layer via EDL gating method, where negative gate voltage is applied to the both carrier-type samples. Negative gate voltage corresponds to tuning the Fermi energy closer to (away from) Dirac line node of CaIrO₃ for n -type (p -type) sample as shown in the top schematics of Fig. 4(a). We performed Hall measurements at several gate voltages. Each gate voltage was applied at 265 K for 60 mins before the samples were cooled down to each measurement temperature at the rate of 0.5 K/min. Before Hall measurements, we confirmed that negative gate voltage reversibly modulated R_S for CaIrO₃ and ruled out the possibility of electrochemical reactions (see supplementary Fig. S2(b)).

Figures 3(a) and 3(b) show B dependence of R_{AHE} at 5 K as a function of gate voltage (V_G) for p - and n -type heterostructures, respectively. The temperature dependence of the R_S is summarized in supplementary Fig. S3. For the n -type heterostructure, negative

V_G increases R_{AHE} . On the other hand, R_{AHE} decreases with negative V_G for the p -type heterostructure. Figures 3(c) and 3(d) show temperature dependence of σ_{xy} at 9 T under several V_G for the p - and n -type heterostructures, respectively. Here, σ_{xy} is calculated as

$$\sigma_{xy} = \frac{R_{\text{AHE}}t}{(R_{\text{St}})^2 + (R_{\text{AHE}}t)^2} \quad (1)$$

where t is the thickness of CaIrO_3 layer. In both heterostructures, the ferromagnetic transition temperature, where the AHE emerges, is unchanged (~ 60 K). Furthermore, the coercive field, which is estimated from the hysteresis loop of R_{AHE} , also remains nearly unchanged against the amplitude of the gate voltage. These results suggest that the magnetic properties of the heterostructures are not modulated by the EDL gating. Rather, the electric field only modifies the carrier density of CaIrO_3 (i.e., the position of the Fermi energy). It should be pointed out that the σ_{xy} calculated from Eq. (1) may be underestimated because the effective thickness accounting for the AHE may be smaller than $t \approx 6$ nm, if we consider the interfacial ferromagnetism arising from proximity effect.

Next, we discuss how CaIrO_3 layer contributes to the AHE. It is well known that AHE is generally classified into two types [23]. One comes from an intrinsic origin where electrons acquire anomalous Hall velocity induced by the Berry curvature in momentum space. This mechanism is dominant in the moderately dirty system where longitudinal conductivity σ_{xx} is below $\sim 10^4$ S/cm. The other comes from an extrinsic origin where electrons are scattered by magnetic impurities via spin-orbit interaction and contribute to the AHE. This mechanism is dominant for larger σ_{xx} above $\sim 10^5$ S/cm. Taking into account that σ_{xx} for our heterostructures is below $\sim 10^3$ S/cm, we can assume that the AHE of the heterostructures comes from the intrinsic origin. At this point, the Dirac-like band dispersion of CaIrO_3 has significance as it can be a source of the Berry curvature. In Kubo formula [24], anomalous Hall conductivity σ_{xy} is given by

$$\begin{aligned} \sigma_{xy} = e^2 \hbar \sum_{n \neq n'} \int \frac{d\mathbf{k}}{(2\pi)^3} [f(\varepsilon_n(\mathbf{k})) - f(\varepsilon_{n'}(\mathbf{k}))] \\ \times \text{Im} \frac{\langle n, \mathbf{k} | v_x(\mathbf{k}) | n', \mathbf{k} \rangle \langle n', \mathbf{k} | v_y(\mathbf{k}) | n, \mathbf{k} \rangle}{[\varepsilon_n(\mathbf{k}) - \varepsilon_{n'}(\mathbf{k})]^2} \end{aligned} \quad (2)$$

where n is band index, $f(\varepsilon_n(\mathbf{k}))$ is Fermi distribution function and $\mathbf{v}(\mathbf{k})$ is velocity operator defined in the \mathbf{k} -dependent Hamiltonian ($H(\mathbf{k})$) for the periodic part of the Bloch functions by

$$\mathbf{v}(\mathbf{k}) = \frac{1}{i\hbar} [\mathbf{k}, H(\mathbf{k})] = \frac{1}{\hbar} \nabla_{\mathbf{k}} H(\mathbf{k}). \quad (3)$$

Equation (2) can be transformed into

$$\sigma_{xy} = -\frac{e^2}{\hbar} \sum_{n \neq n'} \int \frac{d\mathbf{k}}{(2\pi)^3} f(\varepsilon_n(\mathbf{k})) b_n^z(\mathbf{k}) \quad (4)$$

where $b_n^z(\mathbf{k})$ is the Berry curvature. Equation (4) indicates that σ_{xy} is the sum of the Berry curvature over up to the Fermi energy. According to Eq. (2), the anomalous Hall conductivity is enhanced in the following conditions: (i) large group velocity $\mathbf{v}(\mathbf{k})$, which is satisfied in a large band dispersion at the Fermi energy and (ii) two bands are energetically close to each other (i.e., small $\varepsilon_n(\mathbf{k}) - \varepsilon_{n'}(\mathbf{k})$). These two conditions are indeed satisfied when the Fermi energy of CaIrO₃ is tuned close to the Dirac line node.

Figure 4(a) shows gate voltage dependence of σ_{xy} at 5 K. The schematics are also indicated for the Fermi energy relative to the Dirac-like dispersion of CaIrO₃. Both *p*- and *n*-type samples exhibit an almost monotonic increase in σ_{xy} as the Fermi energy approaches the Dirac line node. This trend is consistent with Eq. (2) and our assumption: the AHE in the heterostructures is the intrinsic effect and Dirac-like dispersion of CaIrO₃ contributes to the AHE. Figure 4(b) illustrates our interpretation of the relationship between the band structure of CaIrO₃ and its AHE in the heterostructures. We assume that the degenerated Dirac line node of the CaIrO₃ layer is split into up and down spin bands by the exchange interaction which is induced by the magnetic proximity effect from the CaMnO₃ layer. Although the magnitude of exchange energy is uncertain, it may be several meV order since the AHE commonly emerges at ~ 60 K, or $k_B T_C \approx 5$ meV. Such an induced band splitting results in the band crossings near Dirac line node and the creation of several Weyl nodes as shown in Fig. 4(b). In this study, we assume that the Fermi energy of CaIrO₃ is far above (below) Dirac line node for *n*(*p*)-type samples. It is reported that the Fermi energy for bulk single crystals is about 10 meV above Dirac line node [12]. Since the carrier density of CaIrO₃ films is two orders of magnitude higher than that of single crystals [13], the Fermi energy of our CaIrO₃ layers is estimated to be away from Dirac line node in both carrier-type samples. In this assumption, the negative V_G means that Fermi energy approaches (leaves) the band crossings for *n*(*p*)-type. As the Fermi energy is closer to the band crossings, each carrier acquires larger anomalous velocity from the Berry curvatures, resulting in the enhancement of the AHE (Fig. 4(c)).

In conclusion, we fabricate CaIrO₃/CaMnO₃ heterostructures with both-carrier types and confirm that CaIrO₃ takes the role of the carrier transport in this system. We perform an

electric field control of the AHE emerging at the heterostructures by using EDL gating. In both carrier-type heterostructures, anomalous Hall conductivity is enlarged as a gate voltage tunes the Fermi energy closer to Dirac line node of CaIrO_3 . This result indicates that the AHE comes from an intrinsic origin reflecting the Dirac-like linear energy dispersion of CaIrO_3 . We propose a plausible explanation for the AHE in the context of the Berry curvature originating from Weyl nodes which are presumably induced by the magnetic proximity effect from the CaMnO_3 layer. Our work provides important insight into the origin and manipulation of AHE in the oxide heterointerfaces with Dirac-like band dispersion. Also recently, emergence of Dirac electrons has been reported in strained SrNbO_3 thin films [25, 26], where enhancement of AHE is expected under broken time-reversal and inversion symmetries. In this sense, the demonstrated technique in this report would be a promising way to modulate AHE by not only tuning Fermi level but also breaking inversion symmetry at the interface.

SUPPLEMENTARY MATERIAL

See supplementary material for the additional XRD and transport measurements data.

ACKNOWLEDGMENTS

This work was partly supported by the Japan Science and Technology Agency Core Research for Evolutional Science Technology (JST CREST) (No. JPMJCR16F1) and Izumi Science and Technology Foundation.

DATA AVAILABILITY STATEMENT

The data that support the findings of this study are available from the corresponding author upon reasonable request.

REFERENCES

- ¹H. Y. Hwang, Y. Iwasa, M. Kawasaki, B. Keimer, N. Nagaosa, and Y. Tokura, [Nature Materials](#) **11**, 103 (2012).

- ²Z. Huang, Ariando, X. Renshaw Wang, A. Rusydi, J. Chen, H. Yang, and T. Venkatesan, [Advanced Materials](#) **30**, 1802439 (2018).
- ³P. Yu, W. Luo, D. Yi, J. X. Zhang, M. D. Rossell, C.-H. Yang, L. You, G. Singh-Bhalla, S. Y. Yang, Q. He, Q. M. Ramasse, R. Erni, L. W. Martin, Y. H. Chu, S. T. Pantelides, S. J. Pennycook, and R. Ramesh, [Proceedings of the National Academy of Sciences](#) **109**, 9710 (2012).
- ⁴K. S. Takahashi, M. Kawasaki, and Y. Tokura, [Applied Physics Letters](#) **79**, 1324 (2001).
- ⁵J. Nichols, X. Gao, S. Lee, T. L. Meyer, J. W. Freeland, V. Lauter, D. Yi, J. Liu, D. Haskel, J. R. Petrie, E.-J. Guo, A. Herklotz, D. Lee, T. Z. Ward, G. Eres, M. R. Fitzsimmons, and H. N. Lee, [Nature Communications](#) **7**, 12721 (2016).
- ⁶A. Grutter, B. Kirby, M. Gray, C. Flint, U. Alaun, Y. Suzuki, and J. Borchers, [Physical Review Letters](#) **115**, 047601 (2015).
- ⁷J. W. Freeland, J. Chakhalian, A. V. Boris, J.-M. Tonnerre, J. J. Kavich, P. Yordanov, S. Grenier, P. Zschack, E. Karapetrova, P. Popovich, H. N. Lee, and B. Keimer, [Physical Review B](#) **81**, 094414 (2010).
- ⁸B. R. K. Nanda, S. Satpathy, and M. S. Springborg, [Physical Review Letters](#) **98**, 216804 (2007).
- ⁹S. Bhowal and S. Satpathy, [Physical Review B](#) **99**, 245145 (2019).
- ¹⁰S. Bhowal and S. Satpathy, [npj Computational Materials](#) **5**, 61 (2019).
- ¹¹Z. S. Lim, C. Li, Z. Huang, X. Chi, J. Zhou, S. Zeng, G. J. Omar, Y. P. Feng, A. Rusydi, S. J. Pennycook, T. Venkatesan, and A. Ariando, [Small](#) **16**, 2004683 (2020).
- ¹²J. Fujioka, R. Yamada, M. Kawamura, S. Sakai, M. Hirayama, R. Arita, T. Okawa, D. Hashizume, M. Hoshino, and Y. Tokura, [Nature Communications](#) **10**, 362 (2019).
- ¹³M. Masuko, J. Fujioka, M. Nakamura, M. Kawasaki, and Y. Tokura, [APL Materials](#) **7**, 081115 (2019).
- ¹⁴R. Nishino, Y. Kozuka, M. Uchida, F. Kagawa, and M. Kawasaki, [Applied Physics Letters](#) **112**, 051602 (2018).
- ¹⁵R. Nishino, Y. Kozuka, F. Kagawa, M. Uchida, and M. Kawasaki, [Applied Physics Letters](#) **113**, 143501 (2018).
- ¹⁶R. Nishino, T. C. Fujita, F. Kagawa, and M. Kawasaki, [Scientific Reports](#) **10**, 10864 (2020).

- ¹⁷K. Ueno, S. Nakamura, H. Shimotani, A. Ohtomo, N. Kimura, T. Nojima, H. Aoki, Y. Iwasa, and M. Kawasaki, [Nature Materials](#) **7**, 855 (2008).
- ¹⁸L. Vistoli, W. Wang, A. Sander, Q. Zhu, B. Casals, R. Cichelero, A. Barthélémy, S. Fusil, G. Herranz, S. Valencia, R. Abrudan, E. Weschke, K. Nakazawa, H. Kohno, J. Santamaria, W. Wu, V. Garcia, and M. Bibes, [Nature Physics](#) **15**, 67 (2019).
- ¹⁹P.-H. Xiang, H. Yamada, H. Akoh, and A. Sawa, [Journal of Applied Physics](#) **112**, 113703 (2012).
- ²⁰S. Okamoto, J. Nichols, C. Sohn, S. Y. Kim, T. W. Noh, and H. N. Lee, [Nano Letters](#) **17**, 2126 (2017).
- ²¹D. Hirai, J. Matsuno, D. Nishio-Hamane, and H. Takagi, [Applied Physics Letters](#) **107**, 012104 (2015).
- ²²G. Jackeli and G. Khaliullin, [Physical Review Letters](#) **102**, 017205 (2009).
- ²³S. Onoda, N. Sugimoto, and N. Nagaosa, [Physical Review B](#) **77**, 165103 (2008).
- ²⁴N. Nagaosa, J. Sinova, S. Onoda, A. H. MacDonald, and N. P. Ong, [Reviews of Modern Physics](#) **82**, 1539 (2010).
- ²⁵N. Mohanta, J. M. Ok, J. Zhang, H. Miao, E. Dagotto, H. N. Lee, and S. Okamoto, [Physical Review B](#) **104**, 235121 (2021).
- ²⁶J. M. Ok, N. Mohanta, J. Zhang, S. Yoon, S. Okamoto, E. S. Choi, H. Zhou, M. Briggeman, P. Irvin, A. R. Lupini, Y.-Y. Pai, E. Skoropata, C. Sohn, H. Li, H. Miao, B. Lawrie, W. S. Choi, G. Eres, J. Levy, and H. N. Lee, [Science Advances](#) **7**, eabf9631 (2021).

FIGURES

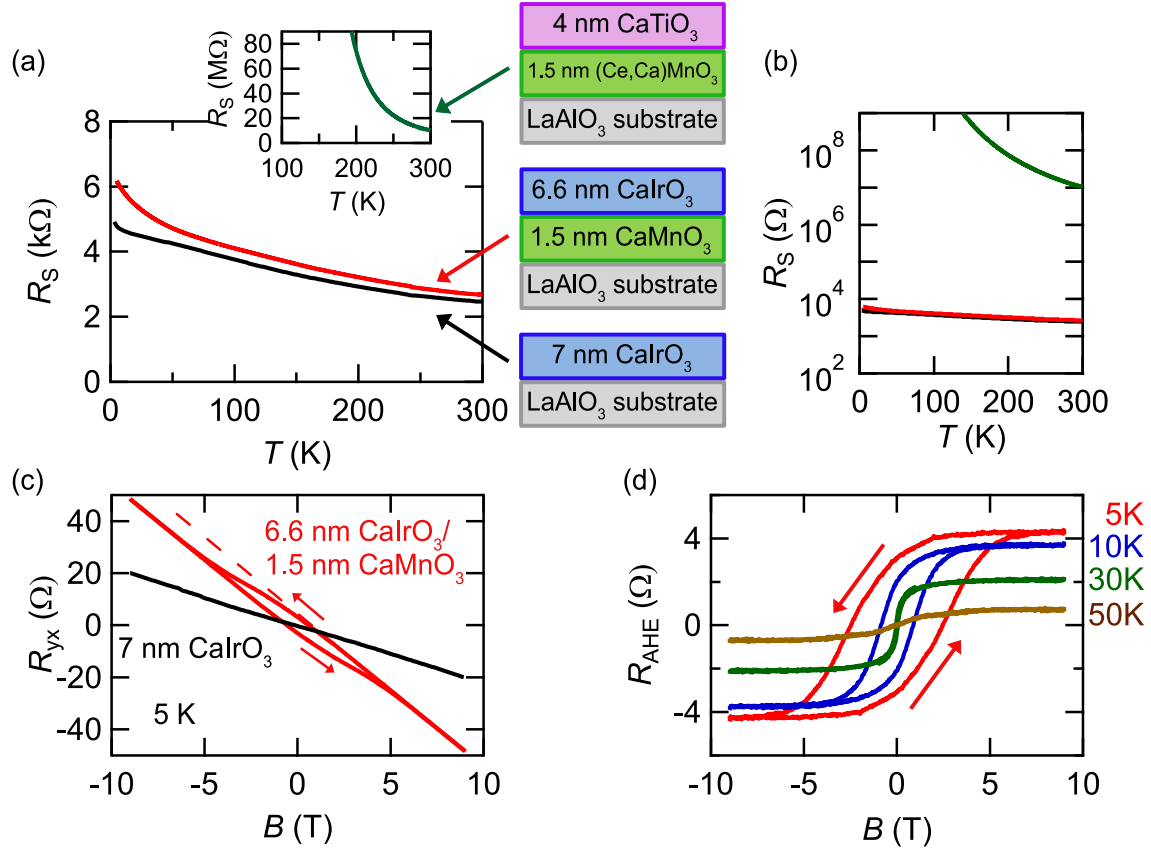


FIG. 1 (Color online). Temperature dependence of sheet resistance (R_S) for $\text{CaIrO}_3/\text{CaMnO}_3$ heterostructure (red) and CaIrO_3 thin film (black) grown on LaAlO_3 substrate. The inset shows R_S for 1.5 nm-thick $\text{Ce}_{0.05}\text{Ca}_{0.95}\text{MnO}_3$ thin film (green) grown on LaAlO_3 substrate as a function of temperature. R_S is displayed in (a) linear and (b) logarithmic scales. Schematics are shown to indicate the structure of each sample as well as the thickness of each layer. (c) Magnetic field (B) dependence of Hall resistance (R_{yx}) for $\text{CaIrO}_3/\text{CaMnO}_3$ heterostructure (red) and CaIrO_3 film (black) at 5 K. The red dashed line represents the linear fitting from the higher magnetic field region. (d) Anomalous Hall resistance (R_{AHE}) of the heterostructure at various temperatures.

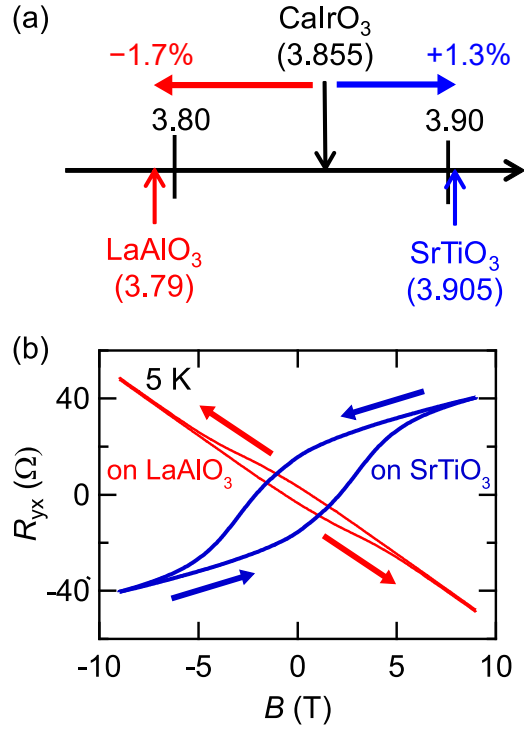


FIG. 2 (Color online). (a) Lattice parameters of CaIrO₃, LaAlO₃ and SrTiO₃ substrates. Those for CaIrO₃ and LaAlO₃ are displayed in a pseudo-cubic setting. The lattice mismatches between CaIrO₃ and the substrates are also indicated. (b) Magnetic field (B) dependence of Hall resistance (R_{yx}) at 5 K for CaIrO₃/CaMnO₃ heterostructures grown on LaAlO₃ (red) and SrTiO₃ (blue) substrates.

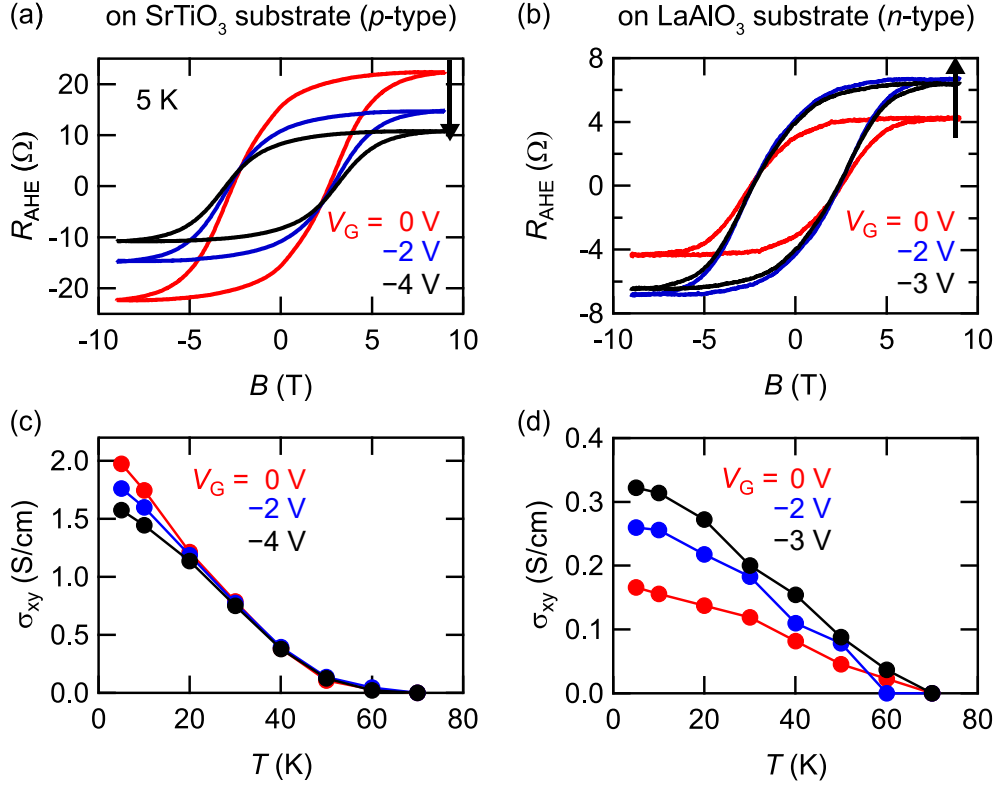


FIG. 3 (Color online). Magnetic field (B) dependence of anomalous Hall resistance (R_{AHE}) at 5 K under several gate voltages (V_G) for (a) p - and (b) n -type samples. Temperature dependence of anomalous Hall conductivity (σ_{xy}) at 9 T under several gate voltages for (c) p - and (d) n -type samples.

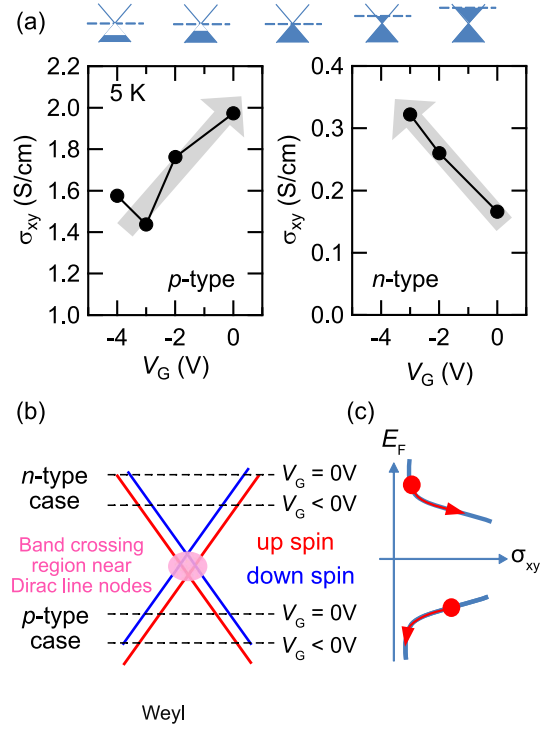


FIG. 4 (Color online). (a) Anomalous Hall conductivity (σ_{xy}) at 5 K as a function of gate voltage (V_G). The top schematics represents a position of the Fermi energy related to Dirac line node of CaIrO_3 . The gray arrows represent a guide to the eye. (b) Illustration for the band structure of CaIrO_3 after band splitting by exchange interaction. Red and blue lines represent up and down spin bands, respectively. (c) Illustration of the relationship between σ_{xy} and position of the Fermi energy, where the crossing point of horizontal and vertical axes indicate the band crossing region in (b).

Supplementary Materials:

Electric field control of anomalous Hall effect in $\text{CaIrO}_3/\text{CaMnO}_3$ heterostructure

I. Reciprocal space mapping for $\text{CaIrO}_3/\text{CaMnO}_3$ heterostructures grown on SrTiO_3 and LaAlO_3 substrates

Figures S1(a) and S1(b) show the reciprocal space mapping images for $\text{CaIrO}_3/\text{CaMnO}_3$ heterostructures grown on SrTiO_3 (1.3% tensile strain) and LaAlO_3 (1.7% compressive strain) substrates, respectively. CaIrO_3 films are fully strained to the substrates in both tensile and compressive strain cases.

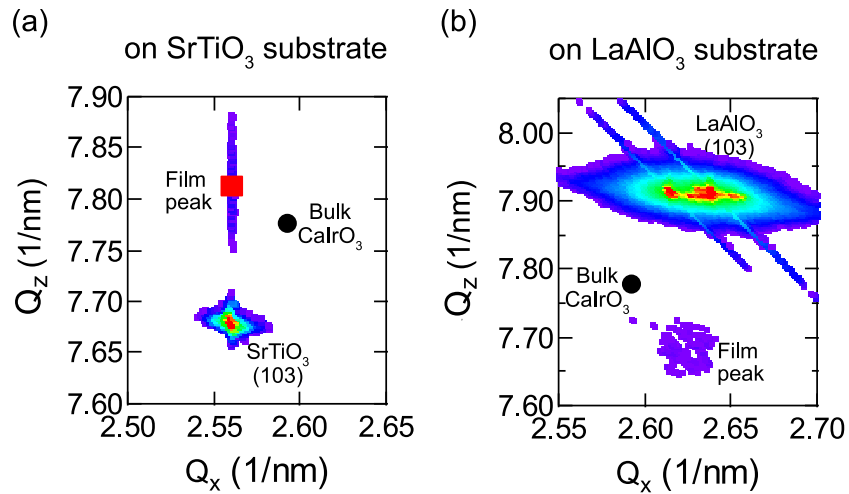


FIG. S1 (Color online). Reciprocal space mappings around (a) SrTiO_3 and (b) LaAlO_3 (103) peaks. Black circle denotes the peak position for the bulk CaIrO_3 calculated from pseudo-cubic lattice constant.

II. Device structure for edl gating and confirmation of no chemical reaction during device operation

Figure S2(a) illustrates a schematic diagram of the device structure for EDL gating. As a gate dielectric, we employed an ionic liquid (IL), N, N-diethyl-N-(2-methoxyethyl)-N-methylammonium tetrafluoroborate (DEME- BF_4), in which a gate electrode of Pt coil is immersed. For the electrical contacts, we utilized Al wire bonding. Al wires are covered

by silicone sealant to preserve a chemical reaction between the IL and Al wires. For the device preparations, we did not use standard lithographic techniques because perovskite iridates are highly prone to be degraded in lithographic processes [S1]. Figure S2(b) shows an example of switching characteristics of the device between gate voltage $V_G = 0$ V and -3 V at 265 K. The reduced sheet resistance (R_S) at $V_G = -3$ V returns to the initial value after gating. This reversible change indicates that EDL gating is an electrostatic modulation of the carrier density and does not cause any electrochemical reactions.

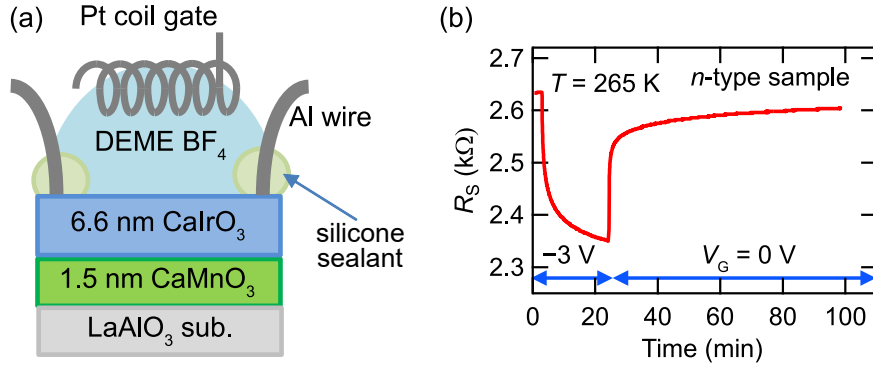


FIG. S2 (Color online). (a) Schematic diagram of the device structure for EDL gating. (b) Time dependence of sheet resistance (R_S) at 265 K for the heterostructure between gate voltage $V_G = 0$ V and -3 V.

III. Temperature dependence of sheet resistance for $\text{CaIrO}_3/\text{CaMnO}_3$ heterostructures as a function of gate voltage

Figures S3(a) and S3(b) show temperature dependence of sheet resistance (R_S) as a function of gate voltage V_G for p - and n -type heterostructures, respectively. Negative V_G reduces the R_S in both carrier-type samples. Since negative V_G is expected to deplete electron carrier, the behavior of the n -type carrier sample seems to be opposite to expectation. We speculate this complex dependence on V_G is related to semimetallic properties of perovskite iridates. In fact, similar response to electric field is reported for SrIrO_3 previously [S2].

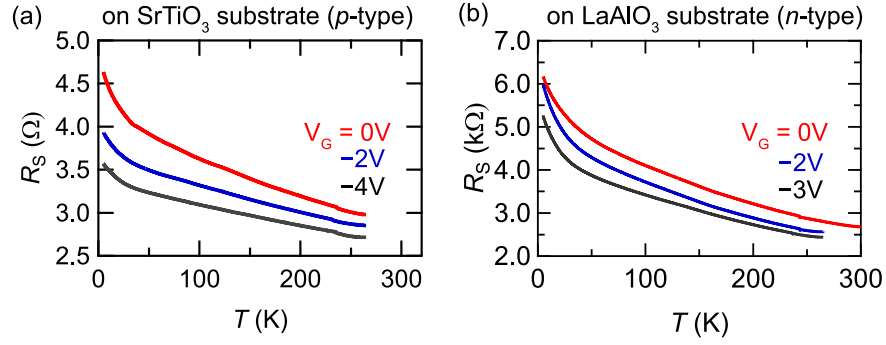


FIG. S3 (Color online). Temperature dependence of sheet resistance (R_s) as a function of gate voltage V_G for (a) *p*- and (b) *n*-type samples.

REFERENCES

- [S1] D. J. Groenendijk, N. Manca, G. Mattoni, L. Kootstra, S. Gariglio, Y. Huang, E. van Heumen, and A. D. Caviglia, [Applied Physics Letters](#) **109**, 041906 (2016).
- [S2] N. Manca, D. J. Groenendijk, I. Pallecchi, C. Autieri, L. M. K. Tang, F. Telesio, G. Mattoni, A. McCollam, S. Picozzi, and A. D. Caviglia, [Physical Review B](#) **97**, 081105 (2018).